Evaluation of the Matrix Structure, Immunological Profile and Cellular Metabolism of Diabetic Breast Cancer Tumors

By

Christopher Andrew Johnson

Thesis

Submitted to the Faculty of the

Graduate School of Vanderbilt University

in partial fulfillment of the requirements

for the degree of

MASTER OF SCIENCE

in

Biomedical Engineering

February 28, 2021

Nashville, Tennessee

Approved:

Dr. Cynthia Reinhart-King, Ph.D

Dr. Todd Giorgio, Ph.D

Table of Contents

List of Figures

List of Abbreviations

AGE	Advanced Glycation End Product
ANOVA	Analysis of Variance
CD	Cluster of Differentiation
DAB	3,3'-Diaminobenzidine
DOC	Sodium Deoxycholate
ECM	Extracellular Matrix
FBS	Fetal Bovine Serum
GLUT1	Glucose Transporter 1
G-418	Geneticin
HEPES	4-(2-hydroxyethyl)-1-piperazineethanesulfonic acid
HRP	Horseradish Peroxidase
IL-6	Interleukin 6
ISDoT	In Situ Decellularization of Tissue
MDSC	Myeloid Derived Suppressor Cell
MMTV-PyMT	Mouse Mammary Tumor Virus Polyomavirus Middle T-Antigen
PBS	Phosphate-buffered Saline
Pen/Strep	Penicillin and Streptomycin
PyMT	Polyomavirus Middle T-Antigen/Non-Diabetic Tumors
qPCR	Quantitative Polymerase Chain Reaction
RAGE	Receptor for Advanced Glycation End Product
SD	Standard Deviation
STZ	Streptozotocin/Diabetic Tumors
TIL	Tumor Infiltrating Lymphocyte
TNF-α	Tumor Necrosis Factor Alpha
2D	Two-Dimensional

2-NBDG	2-(N-(7-Nitrobenz-2-oxa-1,3-diazol-4-yl)Amino)-2-Deoxyglucose
3D	Three-Dimensional

Chapter 1: Introduction

1 in 8 women in the United States will be diagnosed with breast cancer during their lifetime [1]. Despite large advances in the detection and treatment of breast cancer, nearly 43,000 women is the US will die as a result of the disease in 2020 [2]. Breast cancer has also become increasingly prevalent over the last four decades. From 1970 to 2014 the US population rose 57% while the number of new breast cancer cases rose 242%, over 4-fold the population increase, in the same timeframe [1]. There are number of risk factors placing women at a higher risk of developing breast cancer and many also increase the disease's overall mortality. Some of these are non-preventable factors such as age and genetic pre-disposition. However, others such as obesity and diabetes are preventable and clinical interventions exist to mitigate these risk factors [3]. As breast cancer cases continue to rise, it is particularly important we improve our understanding of preventable risk factors and the role they play in promoting the progression of breast cancer with the ultimate goal of reversing their ill effects.

Rates of diabetes in the US are also rising, increasing from 2.52% in 1990 to 13% in 2015, and are expected to continue to rise [4]. This increase is of particular public health concern as diabetes places women at a 20% higher risk of developing breast cancer and up to a 60% higher risk of mortality [5]. Hyperglycemia is the most common side effect of diabetes, and prolonged exposure to hyperglycemia results in a variety of complications such as retinopathy, nephropathy, and neuropathy. However, the mechanisms by which hyperglycemia promotes breast cancer and increases its malignancy is not currently known. High glucose levels can glycate collagen ultimately resulting in crosslinks and stiffening of the extracellular matrix (ECM). This is notable when considering the relationship between diabetes and cancer because stiffer tumors tend be more aggressive across cancers [6]. Previous work done in the Reinhart-King lab with diabetic mouse models shows that diabetic mice develop more aggressive breast cancer pathologies marked by larger and stiffer tumors compared to non-diabetic mice. However, diabetes is a systemic and chronic disease, and its impact on tumor progression likely go beyond stiffening of

the tumor ECM. For example, *in vitro* studies have shown that glycating collagen alters the molecular arrangement and architecture of collagen which can impact cancer cell adhesion and migration [7].

Hyperglycemia may also have second order effects that influence breast cancer progression such as reducing the ability of the immune system to detect and clear tumors. The association between diabetes and immune dysregulation has long been understood, however, what role altered or reduced immunity plays in promoting the formation and progression of breast cancer is unclear [8]. High glucose levels have a direct impact on some immune cells, reducing the anti-tumor efficacy of CD8 T cells and macrophages and promoting leukocyte secretion of interleukin 6 (IL-6) and tumor necrosis factor alpha (TNF-α) which promotes tumor progression and invasiveness [9]. Glycation also promotes the formation of advanced glycation end-productions (AGEs) which promote inflammatory signaling and can ultimately result in aberrant immune signaling and immune cell exhaustion [10]. In addition, there is emerging evidence that increased tumor stiffness may block trafficking of T cell into tumors and also inhibit T cell activation [11-13].

Outside of the impact of diabetes on the ECM and the immune system, hyperglycemia likely has a direct impact on the cancer cells through altering their metabolism [9]. One of the hallmarks of cancer is an increased reliance on glycolysis even in the presence of oxygen which has become known as the Warburg effect [14]. The metabolic impact of the Warburg effect is especially notable because oxidative phosphorylation is 18-fold more efficient than glycolysis in producing ATP [15]. While the Warburg effect has been well documented, the precise fitness benefits it offers and why this metabolic reprogramming emerges across cancers is still debated. In the context of diabetes, the high levels of excess glucose available to tumors may further reinforce this metabolic rewiring and result in selection of unusually glycolytic clones.

Hyperglycemia has a wide range of effects on the ECM, immune system, and cellular metabolism, but the extent to which these factors are relevant in driving the formation and

progression of breast cancer is not clear. Given the rising incidence of both breast cancer and diabetes there is a significant public health motivation to answer these questions. This thesis investigates the impact of diabetes on breast cancer using a diabetic mouse model. Specifically, we will examine diabetic tumors to 1) characterize their collagen alignment and architecture 2) quantify the level of immune infiltration and 3) isolate and characterize primary tumors cells.

Chapter 2: Comparison of Collagen Architecture

2.1. Introduction

Tumor progression is marked by extensive changes to both the ECM and cellular components of the tumor microenvironment. These changes act to support the growth of cancer cells and suppress antitumor immunity [16]. To study how diabetes alters the tumor ECM, previous colleagues in the Reinhart-King lab developed a diabetic spontaneous breast cancer mouse model using MMTV-PyMT mice and streptozotocin (STZ) injections which kills insulin secreting pancreatic beta islet cells and results in a diabetic phenotype characterized by blood glucose levels > 400 mg/dL. Using this mouse model, they found that diabetic mice form larger and stiffer tumors compared to non-diabetic controls. Based on existing data linking tumor stiffness to increased malignancy, we believe that the increased stiffness of diabetic tumors mediates, at least in part, their increased aggressiveness. We also hypothesized that the stiffness is the result of hyperglycemia and the glycation of collagen within the tumor ECM. High glucose is known to crosslink collagen and increase bulk stiffness of the ECM, however, we wanted to know what impact these crosslinks have on collagen architecture and alignment *in vivo*. Increased collagen alignment is a characteristic feature of tumor ECM and is also associated with poor patient outcomes in breast cancer [6, 17]. Therefore, we hypothesized that the crosslinked diabetic tumor ECM would also consist of more highly aligned collagen fibers.

To test our hypothesis that diabetic tumors have a more aligned collagen architecture, we needed to decellularize the ECM without changing its structure or composition. Few methods

meet these requirements, however, *in situ* decellularization of tissue (ISDoT) utilizes an animal's existing veins and arteries to deliver decellularization solutions to specific tissues at controlled flow rates leaving native ECM architecture intact [18].

2.2. Results

After decellularizing and obtaining reflectance images of our tumors, we used CurveAlign and ctFIRE to analyze the images and identify changes in collagen architecture induced by diabetes (Fig. 1a, 1b). In our 2D analysis of diabetic (STZ) and non-diabetic (PyMT) tumor ECM, we found no statistically significant changes in collagen fiber alignment, fiber width, fiber length, or fiber angle (Fig. 1c). The values of the measured parameters also clustered closely between STZ and PyMT tumors with the exception of fiber alignment. Fiber alignment values varied widely within both STZ, mean=0.347 SD=0.273, and PyMT tumors, mean=0.397 SD=0.174, although the values were more uniformly distributed within the PyMT group with a variance of 0.031 compared to a variance of 0.074 in the STZ group (n=15 images of 5 tumors from 5 different mice). The primary drawback involved with using CurveAlign and ctFIRE is the program requires z-stacks, a 3D representation of volume created with 2D images captured at regular intervals in the 3rd or z dimension, to be collapsed into a single image prior to analysis. Since both CurveAlign and ctFIRE are unable to resolve depth, this can result in the artificially increase or decrease fiber alignment outputs depending on how those alignment patterns vary with depth in the imaged tumor.

Given the wide distribution of fiber alignment values, and the two-dimensional nature of ctFIRE and CurveAlign analysis, we wanted to know if collagen fiber alignment was changing with depth from the surface of the tumor. To accomplish this, we utilized an algorithm described by Liu *et al.* 2017 that quantifies three-dimensional collagen organization based on directional variance within and between planes of z-stack images [19]. Despite the sensitivity this method added, we did not find any significant differences in collagen total fiber variance (fiber variance between

planes), local fiber variance (fiber variance within planes), or mean fiber intensity (a measure of signal or collagen density) (Fig. 1d). As tumor progress they re-organize the extracellular matrix often resulting in the linearization and alignment of collagen fibers [20]. Increased collagen fiber alignment, fiber width, and fiber length is associated with increased tumor stiffness and tumor malignancy across a variety of cancers [17, 21, 22].

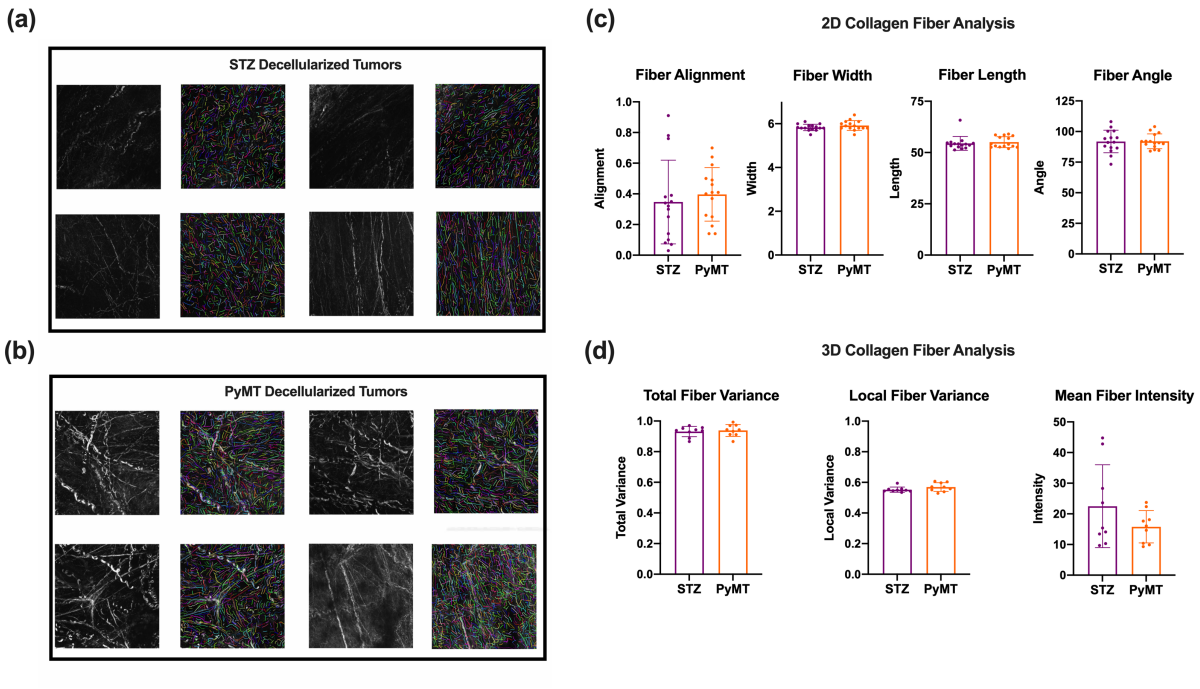

Fig. 1. STZ and PyMT tumors have similar collagen architecture. (**a**) Representative reflectance images of collagen fibers and CurveAlign analysis outputs for decellularized diabetic STZ tumors and (**b**) non-diabetic PyMT tumors. (**c**) CurveAlign analysis of fiber alignment and ctFIRE analysis of fiber width, fiber length, and fiber angle. 15 images were analyzed per group. (**d**) 3D analysis of collagen fiber variance and mean fiber intensity. 9 images analyzed per group. Unpaired two-tailed *t*-tests were used to test for significance between groups. **P≤0.05 threshold for significance.*

2.3. Discussion

Our 2D collagen analysis found no difference in collagen fiber alignment, width, length, and angle between STZ and PyMT tumors (Fig. 1c). This was counter to our hypothesis that STZ tumors would have higher levels of collagen alignment. However, we did observe a wide distribution of fiber alignment measurements within both the STZ and PyMT tumors. We initially believed this was the result of collapsing the entire z-stack into a single image for analysis as this combines all the fibers from the surface up to 150 uM deep into single plane. To overcome this, we adapted a 3D fiber analysis algorithm to differentiate in plane versus between plane fiber variance. Using the 3D analysis algorithm, we observed high levels of total fiber variance in both STZ, mean=0.931, and PyMT tumors, mean=0.938 P=0.683, which quantifies the change in collagen fiber alignment between planes of the z-stack (Fig. 1d). We also observed similar and relatively low levels of local fiber variance in the STZ, mean=0.552, and PyMT tumors, mean=0.569 P=0.14, corresponding to collagen fiber variance at a fixed depth or variance within a plane of the z-stack (Fig. 1c). These findings supported our hypothesis that the wide distribution of fiber alignment values observed in the initial 2D analysis was the result of changes in collagen alignment with depth from the ventral surface of the tumor. Based on these results, there are no significant differences in collagen architecture between STZ and PyMT tumors. However, STZ and PyMT tumors exhibit high levels of fiber variance between planes of the tumor and moderate fiber variance within any single plane. The higher level of collagen fiber alignment within planes as compared to between planes suggests that as STZ and PyMT tumors progress they reorganize the ECM to create rungs or scaffolds of collagen parallel to the tumor surface rather than re-aligning the collagen fibers to radiate from the center to the surface of the tumor.

One challenge we discovered while carrying out these experiments was the regional heterogeneity of fiber architecture within any given tumor. All tumors had highly aligned and highly variable regions of collagen alignment. To avoid selection bias, we only selected pieces of tumor corresponding to the ventral surface of the tumor for imaging and randomly selected 3 regions

per piece for imaging. Given our experience, we suspect that the heterogeneity of collagen architecture even within an individual tumor hinders efforts to identify systemic changes in collagen alignment. An improved way to approach the questions we outlined here would be to scan an entire intact piece of tumor rather than randomly select regions for imaging. As the scanned area becomes larger it becomes easier to identify any normal regional variations in collagen alignment, account for them as noise, and home in on an underlying pattern. However, this approach is technically difficult, requires an automated scanning microscope with reflectance capabilities, and large amounts of processing power making this approach unfeasible for most labs.

2.4. Materials and Methods

2.4.1. MMTV-PyMT Mouse Model

The MMTV-PyMT mouse model is a spontaneous breast cancer model in which the mouse mammary tumor virus (MMTV) long terminal repeat drives mammary specific expression of polyomavirus middle T-antigen (PyMT) leading to the formation of breast cancer tumors around 8 weeks of age. We breed and genotyped MMTV-PyMT mice, separating positive females into cohorts of ten. Five animals underwent streptozotocin injection (70 mg/kg QD for 5 days) at 5 weeks to induce diabetes and the remaining 5 were injected with vehicle (NaCitrate) as non-diabetic controls. To ensure diabetes was fully induced prior to tumor formation, animals were monitored with weekly blood glucose checks via a tail vein bleed and standard glucose monitor. Any animals with a blood glucose < 400 mg/dL after 5 streptozotocin injections were excluded from the study. Tumor size was measured weekly with caliper measurements and recorded. All mice in this study were female as female breast cancer accounts for over 99% of cases. Male MMTV-PyMT mice also do not develop breast tumors until much later in life, if ever, due to the hormone dependence of the MMTV promoter.

2.4.2. Decellularization

At 12 weeks of age, both diabetic and non-diabetic cohorts of mice were euthanized via CO2 inhalation and underwent decellularization of the left mammary fat pad. Decellularization was completed through a procedure called in situ decellularization of tissue (ISDoT) described by Mayorca-Guilani et al. 2017 to retain intact collagen architecture [18]. First, the pectoralis and intercostal muscles were sectioned to open the chest cavity, the thymus was removed to reveal the aortic arch, and the aortic arch was clamped before the left subclavian artery and then the left brachiocephalic vein was clamped using microvascular clamps. The L1 and L2 vertebra were then sectioned to reveal the descending aorta and the descending aorta was catheterized with a 27-gauge needle to start retrograde perfusion of the decellularization solutions. Perfusion was run with a peristaltic pump at .0375 mL/min to prevent vascular rupture and maintain the structure of the ECM. The decellularization process begins with a solution of 1% penicillin/streptomycin + .25% amphotericin B + .25% plasmocin run for 15 minutes to clear blood from the system and prevent contamination. Next, 1% sodium deoxycholate was run for 12 hours followed by distilled water alone for 30 minutes and 1% Triton X-100 for 30 minutes then .1% peracetic acid for 30 minutes and finally distilled water alone for 2 hours. The decellularized fat pad was then surgically extracted and stored in distilled water for analysis. Any tumors on the right mammary fat pad were excised and dissociated to derive primary cell lines described in chapter 4.

2.4.3. 2-Dimensional Collagen Analysis

CurveAlign and ctFIRE were used for the 2D analysis of collagen fibers. The MATLAB package used can be found at https://eliceirilab.org/software/curvealign. ctFIRE extracts individual collagen fibers and returns metrics including fiber angle, fiber length, and fiber width. CurveAlign allows bulk assessment of collagen fiber alignment. Tumors samples were obtained through ISDoT described above. 5 mm X 5 mm squares were cut from the ventral surface of the tumor with a microtome blade, making note of which side corresponds to the surface of the tumor, and placed into the imaging vessel ventral surface side up for imaging. Images were obtained with Zeiss LSM700 confocal laser-scanning microscope in 5 uM increments to 150 uM total depth.

Stacks were collapsed with ImageJ and fed into CurveAlign and ctFIRE for analysis as described by Bredfeldt *et al.* 2014 [23].

2.4.4. 3-Dimensional Collagen Analysis

3D analysis of collagen architecture was carried out as described in Liu *et al.* 2016 and the MATLAB code can be found at engineering.tufts.edu/bme/georgakoudi/publications. Tumor samples and images were obtained as described above in 2.4.3. For 3D analysis non-collapsed z-stacks were fed into the MATLAB package.

Chapter 3: Characterization of Infiltrating Immune Cells

3.1. Introduction

Patients with diabetes have an increased risk of infection, higher infection complication rates, reduced wound healing, elevated rates of cancer, and greater mortality from cancer [8]. How these factors are related is not well understood but taken together they point to immune dysregulation in diabetic patients. Studies in both humans and mice show uncontrolled hyperglycemia increases levels of pro-inflammatory innate immune cells due to oxidative stress and AGE RAGE signaling [24-26]. However, hyperglycemia also pushes these innate immune cells towards a tolerogenic phenotype, and they are less able respond to common antigens, such as LPS, compared to cells from non-diabetic patients [27-29]. Elevated levels of reactive oxygen species associated with hyperglycemia also hampers adaptive immunity resulting in reduced T cell activation and activity [30].

Despite the immune dysfunction observed with diabetes, it is a still a disease characterized by high levels of chronic inflammation which is typically mediated by large populations of innate myeloid immune cells [31]. Given that tumors, in general, are considered to be inflammatory, we wanted to know if this inflammation was exacerbated in diabetic tumors. We hypothesized that STZ tumors contain elevated myeloid populations due to an overactivation of innate inflammatory cells associated with diabetes. The widespread use of immunotherapy for the

treatment of cancer has improved our understanding of the different anti-tumor and pro-tumor immune sub-populations and their association with patient outcome. High levels of tumor infiltrating lymphocytes (TILs), which include both CD4 and CD8 T cells, has emerged as a positive prognostic indicator across a variety of cancers including breast cancer [32-35]. However, the immune system is very complex and reliant on crosstalk between myeloid and lymphoid cells to produce an appropriate and effective anti-tumor response. This crosstalk is mediated by chemokines and cytokines that drive immune cell recruitment and also phenotype [36]. For example, normal levels of inflammation, such as those associated with a cut, are important for the recruitment of myeloid cells which help mediate wound healing and prevent infection. However, pathological levels of inflammation associated with chronic infection, or perhaps diabetes, can result in some myeloid cells differentiating into myeloid derived suppressors cells (MDSCs) which are potent inhibitors of lymphocyte activity [37]. With these factors in mind, we hypothesized that STZ tumors contain lower levels of TILs.

3.2. Results

To determine the overall level of immune infiltration, we first used CD45 to stain STZ and PyMT tumor sections (Fig. 2a,2b). Our staining showed STZ tumors contained significantly fewer CD45+, 14.5%, compared to PyMT tumors, 20.6% P=0.0014 (Fig. 2c). CD45 is a pan-immune cell marker of both myeloid and lymphoid immune cells and these data show a reduction in the total immune cell infiltration. However, tumor progression is most closely linked to reduced lymphocyte infiltration. To determine the number of TILs we stained the tumors with CD8, a marker specific to cytotoxic T cells and some natural killer cells. Here we observed a reduced number of CD8+ cells in STZ tumors, 2.6%, compared to PyMT tumors, 3.6% P=0.0462 (Fig. 2d).

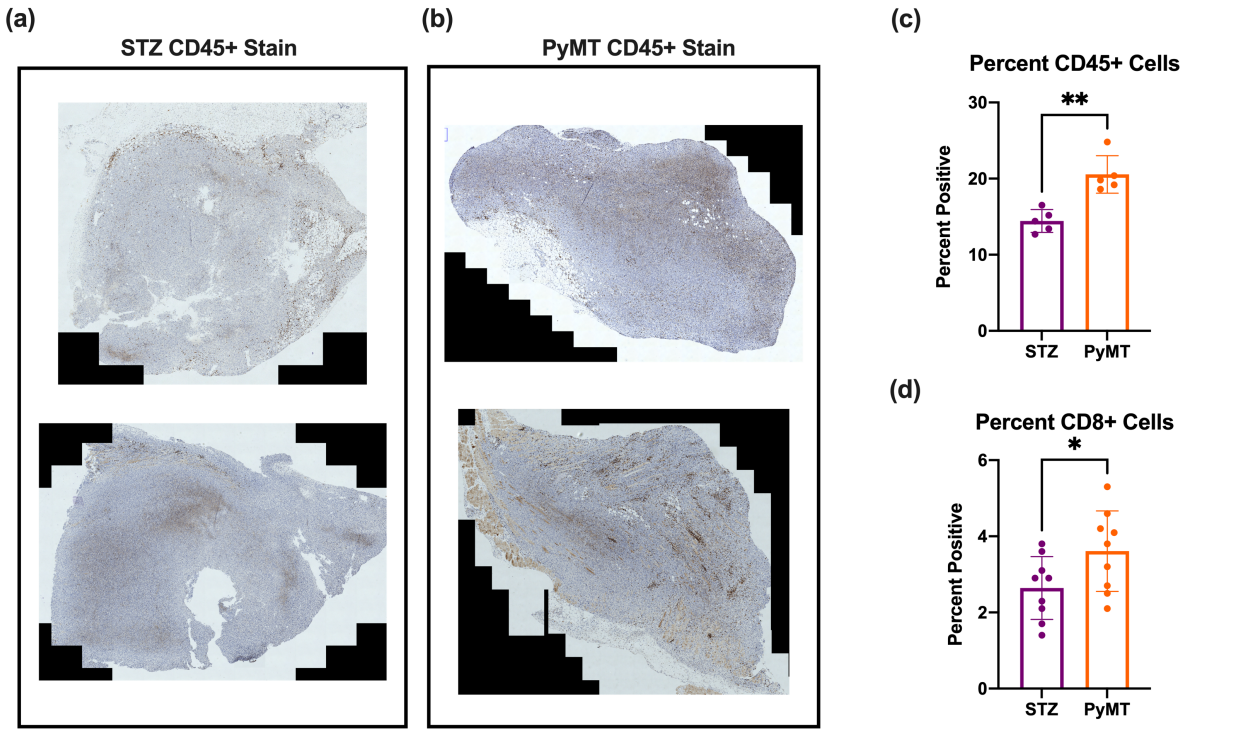

Fig. 2. CD45 and CD8 immune cell populations are reduced in STZ tumors. (**a**) Representative brightfield images of CD45 stained STZ and (**b**) PyMT tumor slides counterstained with hematoxylin. (**c**) Quantification of CD45+ cells as percent of total cells. Five tumors were stained and analyzed per group. (**d**) Quantification of CD8+ cells as percent of total cells. Nine tumors were stained and analyzed per group. Significance determined using unpaired two-tailed *t*-tests. *$P \leq 0.05$, **$P \leq 0.01$.

3.3. Discussion

Our hypothesis that STZ tumors should contain higher levels of tumor infiltrating lymphocytes was based primarily on the fact that hyperglycemia induces high levels of chronic inflammation and these inflammatory cells would infiltrate the tumor due to the tumors itself being an inflammatory environment [38, 39]. However, we saw a statistically significant decrease in the percent of CD45 cells in STZ tumors and this result could be interpreted in a number of ways. First, the data shows a reduction in the total number immune cells but does not indicate what specific immune cell populations are present. Therefore, it is possible that while STZ tumors have fewer immune cells, a large percent of those cells may be inflammatory pro-tumor immune cells.

Another possibility is that large numbers of inflammatory immune cells do infiltrate STZ tumors early on in tumor progression, but the combination of a large influx of immune cells with the already inflamed tumor microenvironment leads to a counterreaction by the immune system to suppress excessive inflammation. This would result in the equivalent of an “off” signal being triggered in the tumor and a reduction in immune cell number and activation.

In Fig. 2d we observed that STZ tumors have a reduced number CD8+ cells as a percent of total cells which aligned with our hypothesis. We observed a reduction in both CD8 and CD45 cell populations, which is consistent with immunosuppression. Whether there is an early influx of inflammatory cells and its contribution to this immunosuppressive phenotype would require additional studies where tumors are taken at early, middle, and late timepoints and stained for CD45 and CD8. Regardless of mechanism, these data shows STZ tumors have reduced CD45 and CD8 populations and suggests immunosuppression may be an additional factor promoting the aggressiveness of STZ tumors. However, analyzing CD45 and CD8 cell populations offers only limited insight into tumor immunity. The immune system is composed of a wide variety of different cells which are further influenced by individual and tumor specific factors. Determining the ratio of regulatory immune cells, such as MDSCs, to cytotoxic lymphocytes in diabetic tumors would provide more insight into the potential role of immunosuppression in diabetic tumor progression. Further work is needed to clarify to what extent diabetes and inflammation alters immunity and what role this might play in tumor progression.

3.4. Material and Methods

3.4.1. Staining

STZ and PyMT tumors were collected and then formalin-fixed and paraffin-embedded prior to sectioning. Slides were deparaffinized in xylene before being rehydrated in a series of graded alcohol. Citrate buffer (10 mM) was used to complete antigen retrieval. Slides from five STZ and five PyMT tumors were then incubated overnight at 4° C with rat anti-mouse CD45

diluted 1:100 (Biolegend #103102) or CD8 antibody diluted 1:50 (Invitrogen #14-0808-82). Anti-rat HRP secondary antibodies and DAB chromogen solution was used for visualization followed by a hematoxylin counterstain. Stained tumors were then scanned on a Leica SCN400 slide scanner in the Vanderbilt Digital Histology Shared Resource Core, and positive cells were counted using QuPATH software (https://qupath.github.io/). Negative controls lacking primary antibody were used to account for any anti-rat HRP or DAB background staining.

Chapter 4: Primary Cell Isolation

4.1. Introduction

After examining the impact of diabetes on the ECM and immune infiltration of STZ tumors, we wanted to understand what affect diabetes has on the cancer cells themselves. Many studies examining the relationship between hyperglycemia and cell behavior utilize standard cancer cell lines such as MDA-MB-231 in hypoglycemic, normal, and hyperglycemic cells lines [40-43]. These studies are useful for understanding the response of cells to changing glucose concentrations but cannot account for the environment in which diabetic tumors evolve [44]. Due to the unique environmental conditions and selective pressures present in the diabetic tumor microenvironment, we hypothesized that diabetic cells should be more reliant on high glucose for basic functions such as proliferation and migration and exhibit elevated levels of glucose transport.

The idea that hyperglycemia induces durable changes in cell phenotype has been explored since the 1980's and has been coined metabolic or hyperglycemic memory [45]. The majority of studies examining metabolic memory have used retinal or endothelial cells due to the prevalence of retinopathy and cardiovascular disease in diabetic patients respectively [46-50]. However, a more recent study by Park *et al.* 2012, also using a diabetic MMTV-PyMT model, provides support for the potential role of metabolic memory in cancer [51]. In Park *et al.* 2012, the authors transplanted tumors from diabetic PyMT mice to non-diabetic PyMT mice. They observed

that diabetic tumors grew faster than non-diabetic tumors even when transplanted into non-diabetic mice. While the mechanisms behind metabolic memory remain under debate, the theory is clinically relevant for diabetic breast cancer patients as it suggests that even with good glycemic control after diagnosis, they retain a higher mortality risk compared to non-diabetic patients.

To test our hypothesis that diabetic cancer cells undergo durable metabolic rewiring during tumor formation, we needed to first isolate primary cell lines from STZ and PyMT mouse tumors. With the primary cell lines established, we could then test such basic parameters as proliferation and migration under various glucose concentrations to determine differential response to glucose within and between cell lines. This simplified model removes other environmental cues cells might otherwise receive in tumor but allows us to focus on the specific impact of glucose on cell behavior.

4.2. Results

To examine any differences in proliferation between STZ and PyMT cell lines, we cultured cells in either 0, 5, 25 or 50 mM glucose media for five days then harvested the cells and quantified the DNA content of each well. 5 mM and 25 mM glucose conditions correspond to normal physiological blood glucose and significant hyperglycemia, respectively, and 50 mM glucose is the highest glucose level cells can be cultured in without exerting osmotic stress on the cells [52]. To account for any differences between 2D and 3D proliferation, we also completed the proliferation assay with cells seeded in 3 mg/mL collagen gels. The common MDA-MB-231 breast cancer cell line was included to provide a benchmark for the proliferative ability and glucose responsiveness of our primary cells. In our 2D assay, the STZ cell line showed a significantly higher rate of proliferation compared to PyMT cells in the 25 mM, $P<0.0001$, and 50 mM glucose conditions, $P<0.0001$, but no difference in proliferation was found in the 0 mM, $P=0.66$ and 5 mM glucose conditions, $P=0.52$ (Fig. 3a). This pattern was replicated in the 3D proliferation assay where cells were seeded in collagen gels (Fig. 3b).

Next we used a scratch assay to determine if there were any differences in migratory ability between the cell lines. STZ cells were significantly more migratory in all glucose concentrations compared to PyMT, 0, 5, 25 mM $P<0.0001$ and 50 mM $P=0.030$ (Fig. 4a). Interestingly, STZ cells reached peak migration under the 5 mM glucose conditions with 25 mM glucose and 50 mM glucose conditions reducing migration, $P=0.002$, and remaining unchanged, $P=0.103$, respectively, and PyMT and MDA-MB-231 cells did not exhibit the same plateau in migration (Fig. 4b).

Scratch assays are a common and convenient way to measure cell migration, however, they are susceptible to the influence of proliferation which can act to push the wound closed. To account for any influence proliferation might have in our migration study, we repeated the scratch assay experiment but included serum free and mitomycin C pre-treatment conditions and reduced the number of media glucose concentrations to 0 mM and 25 mM. Serum starving cells reduces proliferation levels while mitomycin C crosslinks DNA preventing DNA replication and therefore proliferation. The 10% serum group largely replicated our initial experiment, but under serum free conditions STZ cells only achieved higher levels of migration with the addition of glucose (Fig. 4c, 4d).

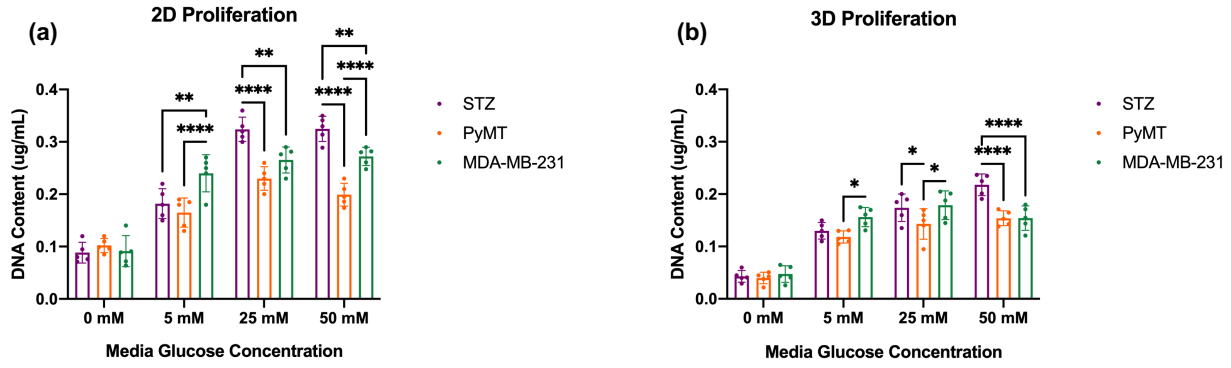

Fig. 3. STZ cells exceed PyMT proliferation rates when glucose is > 25 mM. (**a**) DNA quantification (ug/mL) of cells grown on 24 well plates in specified glucose media for 5 days. (**b**) DNA quantification of cells grown in 3 mg/mL collagen gels in specified glucose media for 5 days. Five replicates per cell line for each glucose concentration. Two-way ANOVA used to test for significant differences between cell lines. *$P\leq0.05$, **$P\leq0.01$, ***$P\leq0.001$.

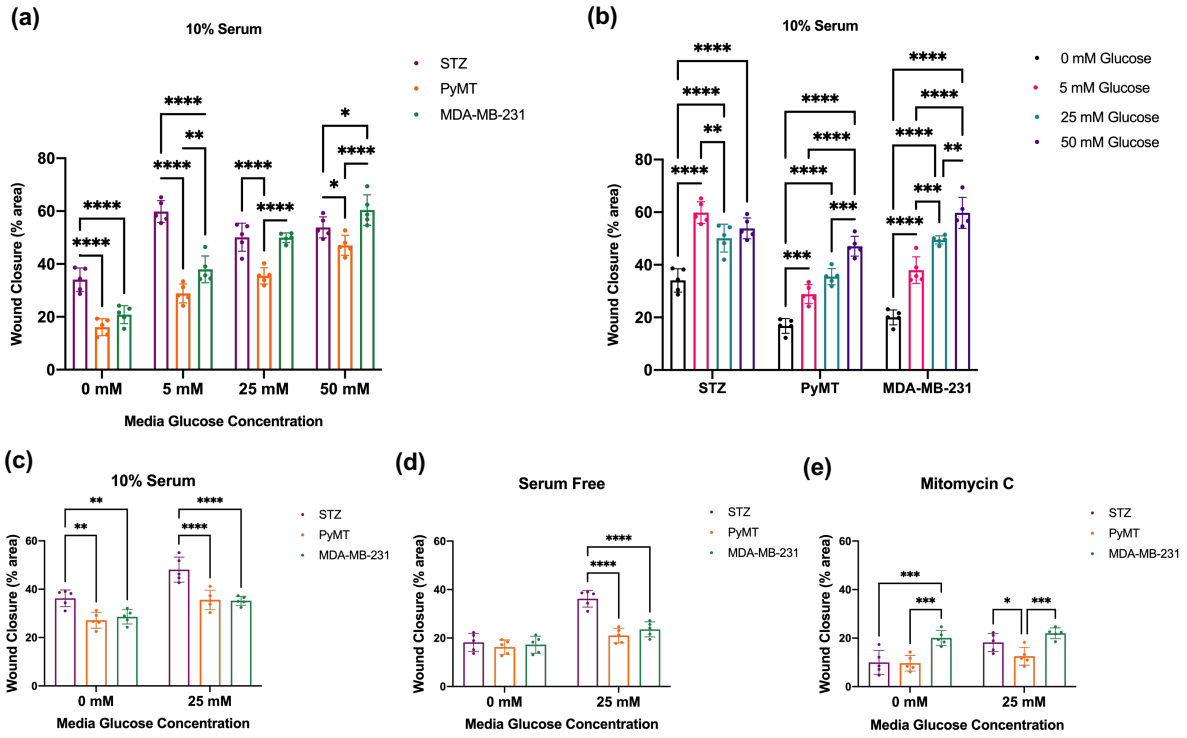

Fig. 4. STZ cells have higher rate of migration independent of media glucose concentration. (**a**) Scratch assay completed in specified glucose media with 10% serum. Wound closure calculated as percent of initial wound area closed 12 hours after scratch. (**b**) Values from Fig. 4a replotted by cell line. STZ cells reach maximum wound closure in 5 mM glucose media. (**c-e**) Scratch assay repeated 10% serum, no serum, and mitomycin C. (**d**) STZ cells lose wound closure advantage in the absence of serum and glucose. The addition of glucose rescues wound closure advantage. (**e**) Mitomycin C pre-treatment equalizes STZ and PyMT wound closure rates only in the absence of glucose. Five replicates per cell line for each glucose condition. Two-way ANOVA used to test for significant differences between cell lines and between glucose conditions. *$P \leq 0.05$, **$P \leq 0.01$, ***$P \leq 0.001$.

Given the trend towards increased migration and proliferation of the STZ cells, we next wanted to dissect out a mechanism. First, we compared the general ability of the cells to produce ATP by comparing the number and the activity of mitochondria. To complete this we seeded cells

and stained them with MitoTracker which localizes to mitochondria and accumulates based on mitochondria membrane potential. The cells were then imaged, and relative fluorescence intensity of staining was measured (Fig. 5a). We observed no difference in MitoTracker staining suggesting STZ and PyMT cells have a similar number of mitochondria and overall mitochondrial activity mean=0.452 SD=0.032 and mean=0.469 SD=0.015 respectively (Fig. 5b). We used a 2-NBDG assay to compare glucose uptake rates between the cell lines and normalized 2-NBDG uptake to DAPI signal to control for any difference in numbers of cells present. We found that STZ cells exhibit a higher level of glucose uptake in both 2D and 3D culture compared to PyMT cells (Fig. 5c, 5d). There are several transporters cell use to uptake glucose, but GLUT1 is the most commonly overexpressed transporter in cancer and has the highest affinity for glucose within the GLUT transporter family [53]. Therefore, we hypothesized that the increased glucose uptake in STZ cells might be mediated by an upregulation of GLUT1. We tested our hypothesis by culturing cells in 0 mM media for 12 hours after which they either remained in 0 mM media or were switched to 5 mM or 25 mM glucose media. Cells were harvested 12 hours and 24 hours after receiving their respective experimental media, mRNA was extracted, and GLUT1 expression levels were determined with qPCR. After 12 hours, we observed a significant increase in GLUT1 expression in STZ cells compared to PyMT for both the 5mM and 25 mM glucose (Fig. 5e). After 24 hours, however, STZ GLUT1 expression was only higher in the 25 mM glucose condition (Fig. 5f).

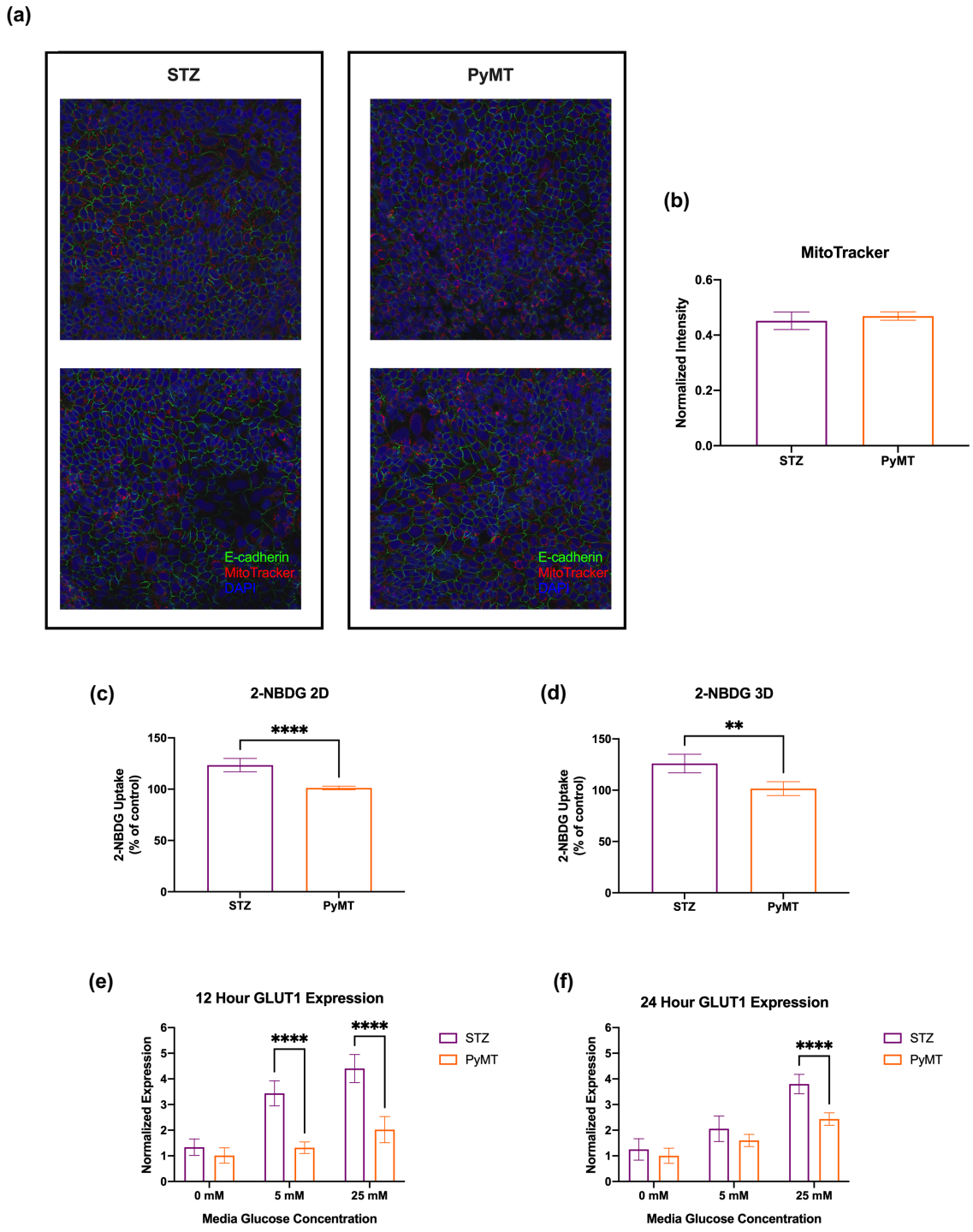

Fig. 5. STZ cells have higher levels of glucose uptake and GLUT1 expression. (**a**) Fluorescent images of STZ and PyMT cells stained with MitoTracker (red) and DAPI (blue). (**b**) Quantification of MitoTracker staining normalized to DAPI of seven STZ and seven PyMT tumors. Significance was tested using an unpaired two-tailed *t*-test. (**c**) Quantification of 2-NBDG staining normalized to PyMT uptake levels in 2D and (**d**) 3D with five replicates per group. Unpaired two-tailed *t*-tests used to determine significance. (**e-f**) qPCR analysis of GLUT1 expression at 12 and 24 hours with expression normalized to PyMT 0 mM expression levels for each timepoint. Six replicates per glucose condition and cell line for both 12 and 24 hour timepoints. Two-way ANOVA used to test for significance. **P*≤0.05, ***P*≤0.01, ****P*≤0.001.

4.3. Discussion

In 25 mM and 50 mM glucose concentrations, STZ cells exhibited significantly higher levels of proliferation compared to PyMT cells. This increase was replicated in both our 2D and 3D proliferation assays. However, we found no difference in proliferation between the two cell lines when cultured under 0 mM and 5 mM glucose conditions. Interestingly, STZ cell proliferation does not increase further when media glucose is raised from 25 mM to 50 mM. This suggests that 25 mM glucose conditions may represent a saturation point where STZ cells are transporting and utilizing glucose at a maximal rate for the purpose of proliferation. A 25 mM glucose saturation also makes sense physiologically as 25 mM is equivalent to 450 mg/dL blood glucose, which is similar to the blood glucose levels of our diabetic mice. We observed a similar pattern when comparing migration between both cell lines. In our scratch assays done with 10% serum, we observed that STZ have a higher level of migration comparted to PyMT regardless of glucose concentration. However, STZ migration plateaus after 5 mM glucose, slightly decreasing at 25 mM and remaining unchanged at 50 mM. The plateau of STZ cell proliferation at 25 mM is likely a result of physical limitations in the transport and utilization of glucose, however, the plateau of STZ migration at a relatively low glucose level is more difficult to explain. One potential explanation is that STZ cells experience stress under the relatively low 5 mM glucose conditions and become more migratory in an attempt to reach regions with more glucose.

Although we found no difference in MitoTracker staining between STZ and PyMT cells, we did find that STZ cells uptake glucose at a significantly higher rate (Fig 4c, 4d). This suggests that STZ cells are utilizing the excess glucose they uptake for glycolysis which occurs in the cytoplasm instead of the mitochondria. We also found that STZ cells rapidly increase GLUT1 expression with the addition of glucose containing media and have much higher levels of GLUT1 expression compared to PyMT cells (Fig. 4e, 4f). The only exception to this increased GLUT1 expression was found after 24 hours of culture in 5 mM glucose media (Fig. 4f). We believe this

is due to the fact that by 24 hours STZ cells have already consumed the majority of glucose leaving very low levels left to uptake. Our hypothesis could be tested experimentally by repeating the experiment but this time adding fresh media to the culture after 12 hours. Adding the fresh media at 12 hours should rescue GLUT1 expression at the 24-hour timepoint.

Overall, the increased migration and proliferation of STZ cells combined with their increased glucose uptake and higher levels of glycolysis supports our hypothesis that the diabetic tumor microenvironment induces durable changes in cell phenotype and metabolism.

4.4. Materials and Methods

4.4.1. Primary Cell Derivation

STZ and PyMT primary cell lines were isolated from a mammary tumor from a MMTV-PyMT diabetic and non-diabetic mice respectively. After extraction the tumor was minced into 5 mm x 5 mm pieces with a microtome blade, washed three times in 1X PBS, added to a 15 mL conical tube containing 1 mg/mL collagenase I (Worthington) with 1% Pen/Strep, and placed on a rocker at 37° C for 1 hour. After 1 hour the cell solution was poured over a 50 uM cell strainer into a 50 mL conical tube to obtain a single cell solution. The single cell solution was then spun down and resuspended in DMEM (Gibco #11054020) with 20% fetal bovine serum and 1% Pen/Strep. 24 hours after plating cells any non-adherent cells were washed off with PBS and media was changed every 24 hours. After 72 hours of culture, culture media was supplemented with G418 at 100 ug/mL and added to the cells for 24 hours to eliminate fibroblasts. After 24 hours, the G418 media was aspirated and standard DMEM added back. G418 treatment continued every 72 hours for an additional 2 rounds of treatment. Standard DMEM (Gibco #11054020) containing glucose was used during initial isolation and culture.

4.4.2. Cell Characterization

After the primary cells were isolated and given G418 treatment to eliminate fibroblasts, the cells were stained with E-cadherin (Fig. 5a) to ensure they were epithelial and not mesenchymal cells. Primary cells were also stained with α-smooth muscle actin, a commonly used fibroblast marker, to verify that all fibroblasts had been eliminated from the cultures.

4.4.3. Culture

After G418 treatment was completed, STZ and PyMT cell lines were cultured in DMEM with 10% FBS and 1% Pen/Strep. Media was changed every 2 days and cells split 1:10 every 3 days.

4.4.4. Proliferation Assay

Cells were seeded into a 24 well plate and allowed to settle for 24 hours. The cells were then washed with PBS and media containing 0, 5, 25 or 50 mM glucose was added. Media was changed every 24 hours and after five days under experimental conditions, 6 days total culture, cells were harvested and DNA extracted for quantification. DNA was isolated using a DNeasy kit (Qiagen) according to the manufacture's protocol. DNA quantification kit (Abcam ab156902) was used to quantify DNA concentration as outlined by the manufacture. Briefly, provided standards were used to create a standard curve. Experimental samples were added to the DNA assay solution and fluorescence measured at Ex. 480-500 and Em. 520-550 nm using a BioTek plate reader. Final DNA concentration was calculated with the following equation $DNA\ concentration\left(\frac{ng}{mL}\right) = \frac{Sample\ RFU - Blank\ RFU}{Sample\ volume\ (uL)\ x\ slope} x\ 100.$

4.4.5. Collagen Gel Preparation

Collagen from rat tail tendons was solubilized in 0.1% acetic acid to produce a stock 10 mg/mL collagen solution. Gels were made by dilution 10 mg/mL stock solution to 3 mg/mL in 0.1% acetic acid. 10X HEPES buffer and cell suspension containing 50,000 cells was added

and mixed. The solution was then neutralized with 1N NaOH at left to polymerize for 1 hour in a cell culture incubator before media was added.

4.4.6. Scratch Assay

STZ and PyMT cells were seeded into 6 well plates in standard DMEM + 10% FBS + 1% Pen/Strep media at a concentration of 500,000 cells/well. After 2 days cultures reached ~85% confluency and were switched to experimental media glucose conditions, after 12 hours the scratch assay was performed, and cells were imaged every 20 minutes for 12 hours. In mitomycin C condition, cells were pre-treated with 10 ug/mL mitomycin C for 2 hours prior to scratch. Cells in the serum free group were washed with 1X PBS and given DMEM + 1% Pen/Strep 12 hours before scratch was performed. Wound closure was calculated as $wound\ closure\ \% = \frac{Initial\ wound\ area}{Final\ wound\ area} x\ 100$. Wound measurements were made via Wound Healing Size Tool available at https://github.com/AlejandraArnedo/Wound-healing-size-tool/wiki.

4.4.7. 2-NBDG and MitoTracker

For MitoTracker and 2-NBDG assays, cells were seeded into 6 well plates at a density of 500,000 cells/well. After 24 hours cells were washed and switched to experimental media glucose conditions for 24 hours. 2-NBDG was given at 100 ug/mL in glucose free media for 15 minutes at 37° C before media was aspirated and fluorescence measurements were taken Ex. 485 and Em. 535 nm. MitoTracker was used at 50 ug/mL and cells were incubated for 30 minutes at 37° C. Cells were then fixed in cold methanol for 10 minutes at -20° C, rinsed in PBS for 5 minutes 3 times. For E-cadherin and DAPI staining, cells were blocked in PBS with 5% goat serum and 0.3% Triton X-100 for 60 minutes at room temperature, blocking buffer was aspirated and cells were incubated in E-cadherin antibody (Cell Signaling #3199) diluted 1:200 overnight at 4°. The next day antibody solution was removed and 300 nM DAPI diluted in PBS was added at room temperature for 5 minutes. Cells were then rinsed in 1X PBS 3 times and imaged with Zeiss LSM-800 at Ex. 579 and Em. 599 nm for MitoTracker and Ex. 490 and Em. 525 nm for E-cadherin.

MitoTracker and DAPI fluorescence intensity was measured using ImageJ and MitoTracker signal was normalized to the DAPI signal for each image and plotted.

4.4.8. GLUT1 qPCR

GLUT1 expression was determined using Bio-Rad CFX96 real-time qPCR machine with a forward primer sequence of GGGCCTGACCTTCGGATATG and a reverse primer sequence of GCTCCTGTTCGAGGCAACT found on PrimerBank (https://pga.mgh.harvard.edu/primerbank/) and GoTaq qPCR mastermix (Promega). Double delta Ct method was used for analysis and expression was normalized to PyMT 0 mM glucose for each graph.

Chapter 5: Conclusion and Future Directions

Based on previous work in the Reinhart-King lab showing STZ tumors are stiffer and have higher levels of collagen crosslinking, we hypothesized they would also have higher levels of alignment due to the physical linkage of collagen fibers. However, the data presented here shows no difference in collagen fiber alignment, width, length, and angle between STZ and PyMT tumors using both 2-dimensional and 3-dimensional methods of analysis. This suggests that while hyperglycemia does glycate and stiffen the tumor ECM it does not result in systemic changes to the collagen architecture. That being said, ISDoT is a powerful tool for dissecting out the role of ECM on cell behavior and there are many future experiments that should be done to better characterize the diabetic ECM. For example, it would be interesting to seed the primary cells established in this work on STZ and PyMT decellularized tumor matrices and examine cell proliferation and migration. If the diabetic ECM alone induces a more proliferative and migratory cell phenotype these experiments would form the rationale for an in-depth molecular characterization of the diabetic ECM. In addition, primary cells could be seeded on decellularized ECM that is glycated *ex vivo* with ribose to isolate the specific impact of collagen glycation on cell behavior.

In this project we also show that STZ tumors have lower levels of CD45 and CD8 immune cell infiltration highlighting immunosuppression as a potential factor in promoting the progression of diabetic tumors. To expand upon this finding, we believe it would be interesting to use flow cytometry to compare CD8, CD4, PDL1, CD11b, and Ly6C immune cell populations. This staining would profile the specific myeloid and lymphoid immune subpopulations present in diabetic tumors and give insight into their state and activity levels. To test the existence of immunosuppression in patients, the same flow cytometry experiment could be run with tumor samples from diabetic and non-diabetic breast cancer patients. Animal studies using diabetic and non-diabetic immunocompromised NOD *scid* gamma (NSG) mice implanted with STZ or PyMT cells could also be done to control for the impact of the immune system on diabetic tumor progression. If immunosuppression is indeed promoting diabetic tumor growth one would expect both diabetic and non-diabetic NSG mice to form similar sized tumors.

In addition to our findings on the impact of diabetes on the ECM and immune cell populations, we also observed that primary cells isolated from STZ tumors have higher rates of proliferation under glucose concentrations ≥ 25 mM and higher levels of migration regardless of glucose levels. These phenotypic changes in cell behavior were further supported by the fact STZ cells exhibit higher levels of glycolysis and glucose uptake likely mediated by an increase in GLUT1. Our migration experiments utilized scratch assays to determine the level of collective migration and additional experiments should be done to confirm the increased single cell migration of STZ cells using a transwell migration assay. This work should also be expanded upon with Seahorse assays to quantify the levels of glycolysis and oxidative phosphorylation occurring in STZ and PyMT cells and confirm STZ cells are in fact using the excess glucose they uptake for glycolysis.

Taken together, the data presented here shows that diabetic tumors have lower levels of immune cell infiltration and that cells derived from diabetic tumors display elevated levels of glucose uptake and glycolysis and are inherently more proliferative and migratory. These results

raise the possibility that diabetic patients may benefit from immunotherapy such as PD-1 to increase the number of tumor infiltrating lymphocytes or drugs against metabolic targets such as GLUT1 [54].

[1] A. P. Schneider, 2nd, C. M. Zainer, C. K. Kubat, N. K. Mullen, and A. K. Windisch, "The breast cancer epidemic: 10 facts," (in eng), *Linacre Q,* vol. 81, no. 3, pp. 244-277, 2014, doi: 10.1179/2050854914Y.0000000027.

[2] R. L. Siegel, K. D. Miller, and A. Jemal, "Cancer statistics, 2020," *CA: A Cancer Journal for Clinicians,* https://doi.org/10.3322/caac.21590 vol. 70, no. 1, pp. 7-30, 2020/01/01 2020, doi: https://doi.org/10.3322/caac.21590.

[3] A. O. Eketunde, "Diabetes as a Risk Factor for Breast Cancer," (in eng), *Cureus,* vol. 12, no. 5, pp. e8010-e8010, 2020, doi: 10.7759/cureus.8010.

[4] C. f. D. C. a. Prevention, "National Diabetes Statistics Report," *Centers for Disease Control and Prevention, U.S. Dept of Health and Human Services,* 2020.

[5] H. K. Bronsveld *et al.*, "Diabetes and Breast Cancer Subtypes," (in eng), *PLoS One,* vol. 12, no. 1, p. e0170084, 2017, doi: 10.1371/journal.pone.0170084.

[6] I. Acerbi *et al.*, "Human breast cancer invasion and aggression correlates with ECM stiffening and immune cell infiltration," (in eng), *Integr Biol (Camb),* vol. 7, no. 10, pp. 1120-1134, 2015, doi: 10.1039/c5ib00040h.

[7] S. Bansode *et al.*, "Glycation changes molecular organization and charge distribution in type I collagen fibrils," *Scientific Reports,* vol. 10, no. 1, p. 3397, 2020/02/25 2020, doi: 10.1038/s41598-020-60250-9.

[8] S. E. Geerlings and A. I. M. Hoepelman, "Immune dysfunction in patients with diabetes mellitus (DM)," *FEMS Immunology & Medical Microbiology,* vol. 26, no. 3-4, pp. 259-265, 1999, doi: 10.1111/j.1574-695X.1999.tb01397.x.

[9] P. Ramteke, A. Deb, V. Shepal, and M. K. Bhat, "Hyperglycemia Associated Metabolic and Molecular Alterations in Cancer Risk, Progression, Treatment, and Mortality," (in eng), *Cancers,* vol. 11, no. 9, p. 1402, 2019, doi: 10.3390/cancers11091402.

[10] S. Son, I. Hwang, S. H. Han, J. S. Shin, O. S. Shin, and J. W. Yu, "Advanced glycation end products impair NLRP3 inflammasome-mediated innate immune responses in macrophages," (in eng), *J Biol Chem,* vol. 292, no. 50, pp. 20437-20448, Dec 15 2017, doi: 10.1074/jbc.M117.806307.

[11] M. Saitakis *et al.*, "Different TCR-induced T lymphocyte responses are potentiated by stiffness with variable sensitivity," (in eng), *Elife,* vol. 6, p. e23190, 2017, doi: 10.7554/eLife.23190.

[12] K. L. Hui, L. Balagopalan, L. E. Samelson, and A. Upadhyaya, "Cytoskeletal forces during signaling activation in Jurkat T-cells," (in eng), *Mol Biol Cell,* vol. 26, no. 4, pp. 685-695, 2015, doi: 10.1091/mbc.E14-03-0830.

[13] E. Judokusumo, E. Tabdanov, S. Kumari, M. L. Dustin, and L. C. Kam, "Mechanosensing in T lymphocyte activation," (in eng), *Biophysical journal,* vol. 102, no. 2, pp. L5-L7, 2012, doi: 10.1016/j.bpj.2011.12.011.

[14] D. Hanahan and Robert A. Weinberg, "Hallmarks of Cancer: The Next Generation," *Cell,* vol. 144, no. 5, pp. 646-674, 2011, doi: 10.1016/j.cell.2011.02.013.

[15] J. Zheng, "Energy metabolism of cancer: Glycolysis versus oxidative phosphorylation (Review)," (in eng), *Oncol Lett,* vol. 4, no. 6, pp. 1151-1157, 2012, doi: 10.3892/ol.2012.928.
[16] M. W. Pickup, J. K. Mouw, and V. M. Weaver, "The extracellular matrix modulates the hallmarks of cancer," (in eng), *EMBO Rep,* vol. 15, no. 12, pp. 1243-1253, 2014, doi: 10.15252/embr.201439246.
[17] M. W. Conklin *et al.*, "Aligned collagen is a prognostic signature for survival in human breast carcinoma," (in eng), *Am J Pathol,* vol. 178, no. 3, pp. 1221-32, Mar 2011, doi: 10.1016/j.ajpath.2010.11.076.
[18] A. E. Mayorca-Guiliani, C. D. Madsen, T. R. Cox, E. R. Horton, F. A. Venning, and J. T. Erler, "ISDoT: in situ decellularization of tissues for high-resolution imaging and proteomic analysis of native extracellular matrix," (in eng), *Nat Med,* vol. 23, no. 7, pp. 890-898, Jul 2017, doi: 10.1038/nm.4352.
[19] Z. Liu *et al.*, "Automated quantification of three-dimensional organization of fiber-like structures in biological tissues," (in eng), *Biomaterials,* vol. 116, pp. 34-47, Feb 2017, doi: 10.1016/j.biomaterials.2016.11.041.
[20] E. A. Brett, M. A. Sauter, H.-G. Machens, and D. Duscher, "Tumor-associated collagen signatures: pushing tumor boundaries," *Cancer & Metabolism,* vol. 8, no. 1, p. 14, 2020/07/02 2020, doi: 10.1186/s40170-020-00221-w.
[21] Z.-H. Zhou, C.-D. Ji, H.-L. Xiao, H.-B. Zhao, Y.-H. Cui, and X.-W. Bian, "Reorganized Collagen in the Tumor Microenvironment of Gastric Cancer and Its Association with Prognosis," (in eng), *J Cancer,* vol. 8, no. 8, pp. 1466-1476, 2017, doi: 10.7150/jca.18466.
[22] K. B. Pointer, P. A. Clark, A. B. Schroeder, M. S. Salamat, K. W. Eliceiri, and J. S. Kuo, "Association of collagen architecture with glioblastoma patient survival," (in eng), *J Neurosurg,* vol. 126, no. 6, pp. 1812-1821, 2017/06// 2017, doi: 10.3171/2016.6.jns152797.
[23] J. S. Bredfeldt *et al.*, "Computational segmentation of collagen fibers from second-harmonic generation images of breast cancer," (in eng), *J Biomed Opt,* vol. 19, no. 1, p. 16007, Jan 2014, doi: 10.1117/1.Jbo.19.1.016007.
[24] D. T. Graves, G. Naguib, H. Lu, C. Leone, H. Hsue, and E. Krall, "Inflammation is more persistent in type 1 diabetic mice," (in eng), *J Dent Res,* vol. 84, no. 4, pp. 324-8, Apr 2005, doi: 10.1177/154405910508400406.
[25] M. Turina, D. E. Fry, and H. C. Polk, Jr., "Acute hyperglycemia and the innate immune system: clinical, cellular, and molecular aspects," (in eng), *Crit Care Med,* vol. 33, no. 7, pp. 1624-33, Jul 2005, doi: 10.1097/01.ccm.0000170106.61978.d8.
[26] C. Y. Shen *et al.*, "Advanced Glycation End Products of Bovine Serum Albumin Suppressed Th1/Th2 Cytokine but Enhanced Monocyte IL-6 Gene Expression via MAPK-ERK and MyD88 Transduced NF-κB p50 Signaling Pathways," (in eng), *Molecules,* vol. 24, no. 13, Jul 4 2019, doi: 10.3390/molecules24132461.
[27] T. S. Ayala, F. H. G. Tessaro, G. P. Jannuzzi, L. M. Bella, K. S. Ferreira, and J. O. Martins, "High Glucose Environments Interfere with Bone Marrow-Derived Macrophage Inflammatory Mediator Release, the TLR4 Pathway and Glucose Metabolism," *Scientific Reports,* vol. 9, no. 1, p. 11447, 2019/08/07 2019, doi: 10.1038/s41598-019-47836-8.
[28] H. Wang, Q. H. Meng, J. R. Gordon, H. Khandwala, and L. Wu, "Proinflammatory and proapoptotic effects of methylglyoxal on neutrophils from patients with type 2 diabetes mellitus," *Clinical Biochemistry,* vol. 40, no. 16, pp. 1232-1239, 2007/11/01/ 2007, doi: https://doi.org/10.1016/j.clinbiochem.2007.07.016.
[29] T. Komura, Y. Sakai, M. Honda, T. Takamura, K. Matsushima, and S. Kaneko, "CD14+ monocytes are vulnerable and functionally impaired under endoplasmic reticulum stress in patients with type 2 diabetes," *Diabetes,* vol. 59, no. 3, pp. 634-43, Mar 2010, doi: 10.2337/db09-0659.

[30] M. A. Moro-García, J. C. Mayo, R. M. Sainz, and R. Alonso-Arias, "Influence of Inflammation in the Process of T Lymphocyte Differentiation: Proliferative, Metabolic, and Oxidative Changes," (in eng), *Front Immunol,* vol. 9, pp. 339-339, 2018, doi: 10.3389/fimmu.2018.00339.

[31] J. I. Odegaard and A. Chawla, "Connecting type 1 and type 2 diabetes through innate immunity," (in eng), *Cold Spring Harb Perspect Med,* vol. 2, no. 3, pp. a007724-a007724, 2012, doi: 10.1101/cshperspect.a007724.

[32] A. Zgura, L. Galesa, E. Bratila, and R. Anghel, "Relationship between Tumor Infiltrating Lymphocytes and Progression in Breast Cancer," (in gre), *Maedica (Bucur),* vol. 13, no. 4, pp. 317-320, 2018, doi: 10.26574/maedica.2018.13.4.317.

[33] G. E. Idos, J. Kwok, N. Bonthala, L. Kysh, S. B. Gruber, and C. Qu, "The Prognostic Implications of Tumor Infiltrating Lymphocytes in Colorectal Cancer: A Systematic Review and Meta-Analysis," *Scientific Reports,* vol. 10, no. 1, p. 3360, 2020/02/25 2020, doi: 10.1038/s41598-020-60255-4.

[34] Q. Fu *et al.*, "Prognostic value of tumor-infiltrating lymphocytes in melanoma: a systematic review and meta-analysis," (in eng), *Oncoimmunology,* vol. 8, no. 7, pp. 1593806-1593806, 2019, doi: 10.1080/2162402X.2019.1593806.

[35] E. Ruffini *et al.*, "Clinical significance of tumor-infiltrating lymphocytes in lung neoplasms," (in eng), *Ann Thorac Surg,* vol. 87, no. 2, pp. 365-71; discussion 371-2, Feb 2009, doi: 10.1016/j.athoracsur.2008.10.067.

[36] J. Galon and D. Bruni, "Tumor Immunology and Tumor Evolution: Intertwined Histories," (in eng), *Immunity,* vol. 52, no. 1, pp. 55-81, Jan 14 2020, doi: 10.1016/j.immuni.2019.12.018.

[37] D. I. Gabrilovich and S. Nagaraj, "Myeloid-derived suppressor cells as regulators of the immune system," (in eng), *Nat Rev Immunol,* vol. 9, no. 3, pp. 162-174, 2009, doi: 10.1038/nri2506.

[38] J. C. Pickup, "Inflammation and Activated Innate Immunity in the Pathogenesis of Type 2 Diabetes," *Diabetes Care,* vol. 27, no. 3, p. 813, 2004, doi: 10.2337/diacare.27.3.813.

[39] S. I. Grivennikov, F. R. Greten, and M. Karin, "Immunity, inflammation, and cancer," (in eng), *Cell,* vol. 140, no. 6, pp. 883-899, 2010, doi: 10.1016/j.cell.2010.01.025.

[40] W. Duan *et al.*, "Hyperglycemia, a Neglected Factor during Cancer Progression," *Biomed Res Int,* vol. 2014, p. 461917, 2014/04/17 2014, doi: 10.1155/2014/461917.

[41] S. Sun, Y. Sun, X. Rong, and L. Bai, "High glucose promotes breast cancer proliferation and metastasis by impairing angiotensinogen expression," (in eng), *Bioscience reports,* vol. 39, no. 6, p. BSR20190436, 2019, doi: 10.1042/BSR20190436.

[42] W. Li *et al.*, "Effects of hyperglycemia on the progression of tumor diseases," *Journal of Experimental & Clinical Cancer Research,* vol. 38, no. 1, p. 327, 2019/07/23 2019, doi: 10.1186/s13046-019-1309-6.

[43] C. Gupta and K. Tikoo, "High glucose and insulin differentially modulates proliferation in MCF-7 and MDA-MB-231 cells," (in eng), *J Mol Endocrinol,* vol. 51, no. 1, pp. 119-29, 2013, doi: 10.1530/jme-13-0062.

[44] M. Shamsi, M. Saghafian, M. Dejam, and A. Sanati-Nezhad, "Mathematical Modeling of the Function of Warburg Effect in Tumor Microenvironment," *Sci Rep,* vol. 8, no. 1, p. 8903, Jun 11 2018, doi: 10.1038/s41598-018-27303-6.

[45] R. L. Engerman and T. S. Kern, "Progression of Incipient Diabetic Retinopathy During Good Glycemic Control," *Diabetes,* vol. 36, no. 7, p. 808, 1987, doi: 10.2337/diab.36.7.808.

[46] H. P. Hammes, I. Klinzing, S. Wiegand, R. G. Bretzel, A. M. Cohen, and K. Federlin, "Islet transplantation inhibits diabetic retinopathy in the sucrose-fed diabetic Cohen rat," (in eng), *Invest Ophthalmol Vis Sci,* vol. 34, no. 6, pp. 2092-6, May 1993.

[47] R. A. Kowluru, "Effect of Reinstitution of Good Glycemic Control on Retinal Oxidative Stress and Nitrative Stress in Diabetic Rats," *Diabetes,* vol. 52, no. 3, p. 818, 2003, doi: 10.2337/diabetes.52.3.818.

[48] M. R. Bono *et al.*, "Characterization of human IFN-gamma response using somatic cell hybrids of hematopoietic and nonhematopoietic origin," (in eng), *Somat Cell Mol Genet,* vol. 15, no. 6, pp. 513-23, Nov 1989, doi: 10.1007/bf01534912.

[49] S. Roy, R. Sala, E. Cagliero, and M. Lorenzi, "Overexpression of fibronectin induced by diabetes or high glucose: phenomenon with a memory," *Proceedings of the National Academy of Sciences,* vol. 87, no. 1, p. 404, 1990, doi: 10.1073/pnas.87.1.404.

[50] M. A. Ihnat *et al.*, "Reactive oxygen species mediate a cellular 'memory' of high glucose stress signalling," *Diabetologia,* vol. 50, no. 7, pp. 1523-1531, 2007/07/01 2007, doi: 10.1007/s00125-007-0684-2.

[51] J. Park, V. R. Sarode, D. Euhus, R. Kittler, and P. E. Scherer, "Neuregulin 1-HER axis as a key mediator of hyperglycemic memory effects in breast cancer," (in eng), *Proc Natl Acad Sci U S A,* vol. 109, no. 51, pp. 21058-21063, 2012, doi: 10.1073/pnas.1214400109.

[52] C. Brocker, D. C. Thompson, and V. Vasiliou, "The role of hyperosmotic stress in inflammation and disease," (in eng), *Biomol Concepts,* vol. 3, no. 4, pp. 345-364, 2012, doi: 10.1515/bmc-2012-0001.

[53] K. Adekola, S. T. Rosen, and M. Shanmugam, "Glucose transporters in cancer metabolism," (in eng), *Curr Opin Oncol,* vol. 24, no. 6, pp. 650-654, 2012, doi: 10.1097/CCO.0b013e328356da72.

[54] N. S. Akins, T. C. Nielson, and H. V. Le, "Inhibition of Glycolysis and Glutaminolysis: An Emerging Drug Discovery Approach to Combat Cancer," (in eng), *Curr Top Med Chem,* vol. 18, no. 6, pp. 494-504, 2018, doi: 10.2174/1568026618666180523111351.

Appendix

A.1. Protocol: In Situ Decellularization of Tissue

1. Place mice under anesthesia and heparinize with 20 units via tail-vein injection
2. Euthanize mouse via CO2 inhalation and ensure death by waiting an additional 5 minutes after CO2 cycle completes.
    a. Cervical dislocation can be used but risks rupturing the vessels in the neck and obstructing access to the heart.
3. Shave chest and abdomen and disinfect with iodine.
4. Make skin incision from lower abdomen to upper neck and dissect skin to expose chest wall.
5. Section pectoralis and intercostal muscles below the 6^{th} rib to provide access for perpendicular sectioning of rib cage. Section the ribs then perform a sternotomy and pin ribs to operating surface.
6. Gently dissect thymus in order to expose aortic arch. Thymus lies directly on top of all major vessels. If any vessel distal to the left subclavian artery is rupture the procedure will not work.
7. Dissect the aortic arch and surrounding vessels free of connective tissue.
8. Clamp or ligate the aortic arch before the left subclavian artery.
9. Clamp left brachiocephalic vein
10. Clamp inferior vena cava
11. Gently section between the L1 and L2 vertebra to expose the descending aorta
12. Catheterize the descending aorta with a 27-33 gauge needle and perform the following perfusions with the peristaltic pump at .0375 mL/min = .5 setting on pump
13. DI water + 1% Pen/Strep + .25% Amphotericin B + .25% Plasmocin for 15 minutes
14. .5-1% DOC for 12 hours
15. DI water alone for 30 minutes
16. 1% Triton X-100 in DI water for 30 minutes
17. .1% peracetic acid for 30 minutes
18. DI water alone for 2 hours
19. Matrix can be stored in DI water at 4 degrees for over 6 months

A.2. Protocol: Tumor Dissociation

1. Dissect the tumor away from surrounding skin above and mammary fat pad below
2. Cut tumor into 5 mm x 5 mm pieces using microtome blade and wash three times in 1X PBS
3. Place tumor in 15 mL conical tube with 1 mg/mL collagenase I and 1% Pen/Strep and incubate on rocker for 1 hour at 37° C
4. Filter cell solution over 50 uM cell strainer to obtain a single cell solution
5. Spin down cells at 1,000 RPM for 5 minutes
6. Resuspend cell pellet in PBS
7. Spin down cells again at 1,000 RPM for 5 minutes
8. Resuspend and plate cells in DMEM with 20% FBS and 1% Pen/Strep
9. After 24 hours wash off non-adherent cells with 1X PBS and replenish media
10. 48 hours later wash cells with 1X PBS and replace media with DMEM with 20% FBS plus 1% Pen/Strep and G418 at 100 ug/mL for fibroblast elimination
11. After 24 hours in G418 supplemented media wash cells in 1X PBS and replace with standard DMEM with 20% FBS and 1% Pen/Strep
12. Leave cells in standard media for 72 hours before repeating treatment with G418 supplemented media
13. Repeat steps 11 and 12 again

(a)

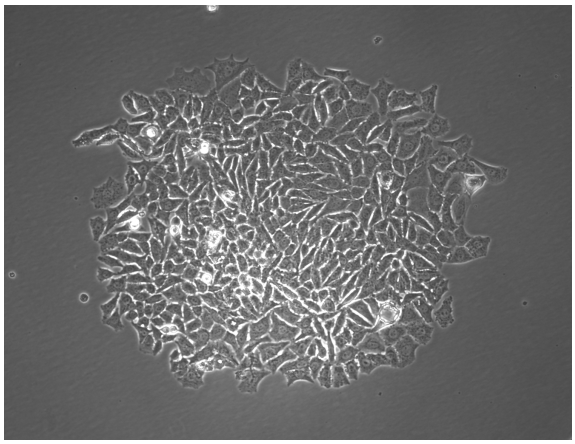

(b)

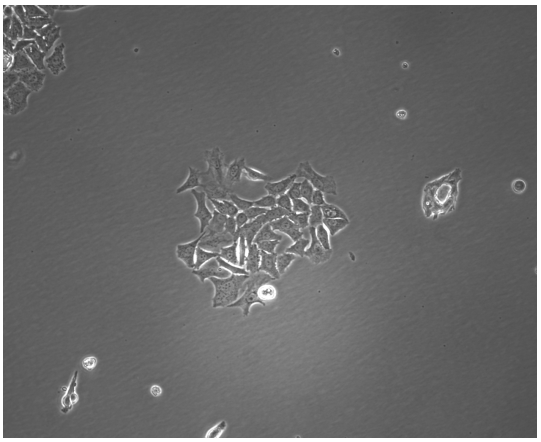

A.2. Images of (**a**) STZ cells and (**b**) PyMT cells 72 hours after isolation.